Magnetic resonance imaging method based on magnetic susceptibility effects to estimate bubble size in alveolar products: application to bread dough during proving.

François de Guio, Maja Musse, Hugues Benoit-Cattin, Tiphaine Lucas, Armelle Davenel

Magnetic resonance imaging method based on magnetic susceptibility effects to estimate bubble size in alveolar products: Application to bread dough during proving

François De Guio [a,b,*]

Maja Musse [a,b]

Hugues Benoit-Cattin [c]

Tiphaine Lucas [a,b]

Armel Davenel [a,b]

[a] *Cemagref, UR TERE, 17 avenue de Cucillé, 35 044 Rennes, France*

[b] *Université européenne de Bretagne, France*

[c] *CREATIS, UMR CNRS 5220, Inserm U630, Université Claude Bernard Lyon 1, INSA Lyon, Bât. Blaise Pascal, 69 621 Villeurbanne, France*

* Corresponding author. E-mail address: francois.de-guio@cemagref.fr

Abstract

Magnetic resonance imaging has proven its potential application in bread dough and gas cell monitoring studies, and dynamic processes such as dough proving and baking can be monitored. However, undesirable magnetic susceptibility effects often affect quantification studies, especially at high fields. A new low field method is presented based on local assessment of porosity in spin-echo imaging, local characterization of signal loss in gradient-echo imaging and prediction of relaxation times by simulation to estimate bubble radii in bread dough during proving. Maps of radii showed different regions of dough constituting networks which evolved during proving. Mean radius and bubble distribution were assessed during proving.

Key Words: magnetic susceptibility; MRI simulation; field inhomogeneity; gas bubble; gas cell; bread; dough; proving; fermentation

1. Introduction

Magnetic susceptibility effects are of increasing interest in Magnetic Resonance Imaging (MRI). Traditionally, as field inhomogeneities induce geometry and intensity distortions in spin-echo (SE) imaging and signal loss in gradient-echo (GE) imaging [1, 2], susceptibility artefacts have been considered undesirable and therefore subjected to correction [3]. However, there are number of emerging techniques and applications using magnetic susceptibility effects and T_2*-weighted imaging. The difference in magnetic susceptibility between deoxygenated and oxygenated blood, termed the BOLD effect, led to functional MRI which is widely used in cognitive neuroscience [4]. Susceptibility Weighted Imaging (SWI) uses the original phase image to enhance contrast between tissues with different susceptibilities [5]. This technique has been applied to studies of brain tumors, trauma, vascular malformations and for quantification of brain iron [6]. Superparamagnetic iron oxide (SPIO) particles create intense magnetic field distortions within and around cells, leading to irreversible signal dephasing in GE sequences. SPIO particles have been exploited as contrast agents for non-invasive cell tracking to determine their biodistribution in different organs [7-10]. Susceptibility studies have been applied to material characterization [11, 12] and particle identification in industrial systems [13].

The potential of gas microbubbles as an in vivo intravascular susceptibility contrast agent for MRI has been demonstrated [14]. Moreover, differences in magnetic susceptibility ($\Delta\chi$) between gas bubbles and a water environment create field inhomogeneities which induce intravoxel dephasing and associated signal loss characterized by a T_2* shortening in GE imaging. However, the presence of air bubbles in several food products has not to date been the focus of studies of susceptibility effects. Understanding bubble mechanics is very important with a wide range of foamed food products. Bubble studies make possible the optimization of process design, contribute to the development of strategies for deaeration and

are important in the area of texture and sensory analysis [15]. It can be anticipated that air or gas bubbles would be natural markers or contrast agents. Moreover, bubbles are part of a product and thus could be considered as a signature of the medium.

Proving flour dough is an essential stage in breadmaking. As the final character of most bakery products depends on the creation and control of gas bubble structures in the unbaked matrix, improving the understanding of the nucleation and growth of bubbles is of major interest [16]. MRI is a particularly suitable tool to study bread dough as it is non-invasive (essential for dough monitoring during proving as the alveolar structure is fragile and may collapse if intrusive measurement techniques are used), and provides a good trade-off between spatial and time resolution [17-20]. Dough samples can thus be quite large and imaged with high resolution during proving [20]. Even the entire baking process can be monitored with MRI [21]. Bonny et al. [17] used high-field (9.4 T) magnetic resonance microscopy along with routine mathematical morphology to characterize the proving process noninvasively. They faced critical susceptibility effects responsible for severe geometrical distortions due to the heterogeneous structure characterized by many interfaces. Different stages of fermentation could be identified, with a general increase in bubbles, but no quantitative assessment of bubble size could be made. Van Duynhoven et al. [20] illustrated the ability of MRI and image analysis to assess gas cell development in the growth of the dough during proving. Basically, the size of each cell was determined by counting the number of pixels, thus presupposing high resolution and hence small fields of view. Moreover, this method does not account for susceptibility effects that are especially disrupting at 4.7 T and are responsible for geometry and intensity distortions in SE imaging. X-ray tomography has also proved its ability in analyzing bubble growth during bread making [22]. However, this technique is only sensitive to density, and imaged samples have to be small (< 10 mm).

The aim of the study reported here was to characterize the alveolar structure of bread dough and its evolution during proving using susceptibility effects. Grenier et al. [18] assessed local dough porosity (volume of gas per volume of dough) during proving. However, nothing can be inferred about bubble size for a given value of porosity, as different cell distributions can be obtained [23, 24]. We therefore developed an original method to estimate bubble size based on the local porosity assessed in SE imaging and on the susceptibility effects in GE imaging. MRI simulation was used to predict signal loss for virtual networks of gas bubbles embedded in a water matrix. A low magnetic field (B_0 = 0.2 T) was used in order to avoid the severe geometric distortions encountered at high field in SE imaging and critical signal losses in GE imaging as the heterogeneous structures were characterized by many susceptibility interfaces [17]. The dynamic side of bread proving requires acquisition to be quite fast, leading to a limited number of acquisitions, limited resolution and an appropriate hypothesis to compute maps of interest.

Section 2 reports how relaxation times affected by susceptibility were predicted with simulation. Section 3 describes the materials and methods used with bread dough preparations, the MRI protocol, computation of the maps and the principle of the estimation algorithm. Section 4 presents the results on non-yeasted bread dough and yeasted dough during proving, followed by a discussion in section 5.

2. Prediction of relaxation times by simulation

The algorithm developed for estimation of bubble size was partly based on simulation results. This section introduces theoretical considerations and describes the simulation protocol. We demonstrate how relaxation times can be modeled at 0.2 T and what can happen at 1.5 T.

2.1. Theoretical considerations

We first verified that the static dephasing regime conditions for spherical magnetic perturbers of radius r as described by Yung et al. [25] were largely met, as $1/\tau << \delta\omega$ with $\tau = r^2/D$ and $\delta\omega = \gamma\Delta\chi B_0/3$, D being the translational diffusion coefficient of spins taken as the water diffusion coefficient and γ the proton gyromagnetic ratio. In fact, D is even smaller in bread dough.

Microscopic field inhomogeneities (i.e. magnetic field inhomogeneities over distances with orders of magnitude smaller than the voxel size) are responsible for irreversible signal decay ($R_2 = 1/T_2$) and mesoscopic field inhomogeneities (from perturbers smaller than the voxel size but greater than the diffusion length) contribute to $R_2^{\#}$, the reversible portion of R_2^* ($R_2^* = R_2 + R_2^{\#} = 1/T_2^*$) [3, 26]. Macroscopic field inhomogeneities are not present in T_2^* definition and induce non-exponential signal decay [3, 27]. Macroscopic field inhomogeneities can typically arise from air inclusions or ferromagnetic objects. Finally, assuming a constant proton density across the voxel ($\rho(\mathbf{r}) = \rho$), signal decay in a voxel of volume V is expressed in Eq. (1):

$$S(t)_{voxel} = \rho/V.e^{-R_2^* t}.\mathrm{sinc}(\gamma t g_x l_x/2).\mathrm{sinc}(\gamma t g_y l_y/2).\mathrm{sinc}(\gamma t g_z l_z/2) \quad (1)$$

where l_x, l_y, l_z are the voxel dimension, and field inhomogeneities along one direction i are expressed with a linear gradient ($\Delta B_i = g_i.i$). In this study, we defined $T_2\chi$ as the constant of the exponential curve fitting the initial part of the susceptibility-induced signal decay. Microscopic, mesoscopic and macroscopic inhomogeneities were thus taken into account in the approximation of $T_2\chi$.

2.2. Simulation protocol

The purpose of the simulation was to investigate quantitatively the signal loss in GE MR images induced by networks of gas bubbles embedded in water. We used the SIMRI MRI

simulator as described by Benoit-Cattin et al [28]. In a previous study [27], intravoxel modeling and associated signal decay were quantitatively assessed and experimentally validated in the case of a single well-resolved air-filled cylinder and in the case of a network of small interacting air-filled cylinders. An overview of the simulation framework is presented in Fig. 1. A 3D virtual object was defined by radius (r) and center to center distance between bubbles (ccd) expressed in pix_{obj} (i.e. the pixel in the 256^3 object space), difference in magnetic susceptibility ($\Delta\chi$) and number of bubbles in each dimension (Nb). The additive property of the magnetic field, and the analytical formulation of field inhomogeneities created by one sphere [1], were combined to compute the relative field inhomogeneities ($\Delta B/B_0$). From this map, SIMRI provides simulated MR images with susceptibility effects. At this stage, object parameters such as spin-lattice relaxation time T_1, spin-spin relaxation time T_2, and proton density ρ could be defined. NMR experiments (Minispec PC 120, Bruker SA, Wissembourg, France) on the bread dough showed several T_1 and T_2 components leading to multi-exponential decay, as previously described [29, 30]. The first components were smaller than the echo times (TE) used in this study. As a single value for relaxation times is necessary in simulation, weighted averaging of the relaxation times of the different components was performed, resulting in T_1 = 100 ms and T_2 = 20 ms. Lodi et al. [31] assessed T_2 values from spin-echo images by fitting time-series points pixel-by-pixel, resulting in T_2 maps of soy bread (mean values around 18 ms) consistent with this averaging. Simulation parameters such as main magnetic field (B_0 = 0.2 T), pixel bandwidth (BW = 279 Hz/pixel) and repetition time (TR = 300 ms) were set to match real experimental conditions. By defining the number of pixels constituting the simulated image, we could define the relative proportion of the bubble radius in the simulated image pixel (pix_{ima}). For instance, considering the high-resolution object used as an example in Fig. 1 (r = 4 pix_{obj}, ccd = 12 pix_{obj}, $\Delta\chi$ = -9.05 ppm, Nb = 17 in the 256^3 object space), a 32x32 slice simulated image resulted in r = 0.5 pix_{ima}, ccd = 1.5

152 pix_{ima} (r = 0.125 pix_{ima}, ccd = 0.375 pix_{ima} with a 8x8 simulated image). For each object, GE
153 images were simulated at different increasing TE from 4 to 12 ms. The mean gray level was
154 then computed on regions of interest (ROI) enclosing several bubbles (visible on Fig. 1). This
155 centred ROI made it possible to avoid boundary effects and to account for the interactions
156 between several bubbles. Good representation of the medium was thus assured with such an
157 ROI as bubbles were regularly spaced. $T_2\chi$ was calculated as the constant of the exponential
158 curve fitting the initial part of the mean gray level decay computed in the ROI. In fact, objects
159 with large ccd gave quasi-exponential decay even for longer TE (12 ms). As ccd decreased,
160 signal decay was hardly exponential because of high gradients g_i in Eq. (1) and $T_2\chi$ was
161 assessed on the very first TE values (between 4 and 8 ms).

162 *2.3. Evolution of $T_2\chi$ as a function of bubble radius*

163 Our aim was to link the object configuration with $T_2\chi$ values so as to characterize the
164 medium. The initial question was to find out whether small or large intravoxel bubbles
165 engendered a similar signal loss for the same porosity (i.e. the gas volume fraction in the
166 voxel). We therefore gathered all $T_2\chi$ values relative to the different object configurations as a
167 function of bubble radius at the different porosities shown in Fig. 2.a. The same curve shape
168 was observed for each porosity. The first plateau indicated that a similar initial signal loss was
169 measured for small radii, i.e. $T_2\chi$ was only dependent on porosity. Then, a rapid increase in
170 $T_2\chi$ leveled off on a second plateau; note that the lower the porosity the smaller the radii
171 corresponding to $T_2\chi$ values as they started to increase. This was appropriate to our study as
172 the initial mean porosity of bread dough was around 10% and overall porosity and bubbles
173 increased during proving. One significant feature was that $T_2\chi$ was sensitive to porosity and
174 intravoxel structure according to bubble size.

175 *2.4. Modeling of $T_2\chi$ at 0.2 T*

176 $T_2\chi$ as a function of bubble radius was modeled with a sigmoid curve for each porosity
177 value; a typical sigmoid function being defined in Eq. (2).

178 $$f(x) = \frac{1}{1+e^{-\lambda x}} \quad (2)$$

179 As curves were not centered but shifted along the radius axis, we defined r_{break} as the
180 radius corresponding to the symmetrical point of the curve. As the amplitude between low
181 and high radius values was not 1, K was introduced as multiplying factor. Finally, $T_2\chi_{init}$ was
182 defined as $T_2\chi$ offset, i.e. the value of $T_2\chi$ for the smallest radius. Using these new variables
183 and Eq. (2), $T_2\chi$ as a function of radius is expressed in Eq. (3):

184 $$T_{2\chi}(r) = T_{2\chi init} + K.\frac{1}{1+e^{-\lambda(r-r_{break})}} \quad (3)$$

185 For several porosity values, the parameters of Eq. (3) ($T_2\chi_{init}$, K, r_{break}, λ) were assessed
186 to best fit the data according to the least mean square criterion (using Marquardt's algorithm
187 in TableCurve2D® software, Jandel Scientific, version 5). Each parameter separately was
188 then studied as a function of porosity. $T_2\chi_{init}$ and K (Fig. 3.a), r_{break} and λ (Fig. 3.b) were
189 drawn up and found to be closely related to porosity with second order polynomial functions
190 (R^2 ($T_2\chi_{init}$) = 0.995, R^2 (K) = 0.988, R^2 (r_{break}) = 0.994 and R^2 (λ) = 0.993).

191 Finally, a complete description of $T_2\chi$ as a function of radius and porosity (ε) is
192 expressed in Eqs. (4,5).

193 $$T_{2\chi}(r,\varepsilon) = T_{2\chi init}(\varepsilon) + K(\varepsilon).\frac{1}{1+e^{-\lambda(\varepsilon)(r-r_{break}(\varepsilon))}} \quad (4)$$

194 With
$$\begin{aligned} T_{2\chi init}(\varepsilon) &= 27.1\varepsilon^2 - 37.1\varepsilon + 17.2 \\ K(\varepsilon) &= -52.9\varepsilon^2 + 49.3\varepsilon - 4.2 \\ \lambda(\varepsilon) &= 133.9\varepsilon^2 - 127.5\varepsilon + 63.6 \\ r_{break}(\varepsilon) &= -1.1\varepsilon^2 + 1.9\varepsilon + 0.2 \end{aligned} \quad (5)$$

Note that the polynomial fitting on K as a function of ε was accurate and determined for porosity values greater than 10%. It was obvious that a homogeneous object without bubbles ($\varepsilon = 0$) would normally result in a zero multiplying factor (K). The same was valid for r_{break}, whose limit for low porosities should be zero. Moreover, zero porosity in the $T_2\chi_{init}$ expression corresponded to the T_2* value, i.e. the exponential signal decay constant representing the signal loss due to the mesoscopic field inhomogeneities.

2.5. Signal losses at 1.5 T

Although a low magnetic field was used, we felt that it could be of interest to predict signal losses in simulation at a higher field. The same simulations were therefore undertaken at 1.5 T and the results are summarized in Fig. 2.b. Susceptibility was obviously stronger as field inhomogeneities were proportional to the main magnetic field. When porosity was equal, $T_2\chi_{init}$ times were considerably shortened compared to the situation at $B_0 = 0.2$ T. Indeed, if $\varepsilon = 0.12$, simulations gave the followings: $T_2\chi_{init} = 12.65$ ms at $B_0 = 0.2$ T and $T_2\chi_{init} = 3.8$ ms at $B_0 = 1.5$ T. The value of B_0 did not seem to impact on r_{break} value. However, the K factor was significantly increased (1.35 at $B_0 = 0.2$ T against 5.11 at $B_0 = 1.5$ T if $\varepsilon = 0.12$). Signal decay was dramatically decreased for higher porosities ($\varepsilon > 0.2$), preventing GE studies at high fields.

We have shown in this section that $T_2\chi$ relaxation time could be modeled with a sigmoid function dependent on porosity and radius of bubbles. We therefore used Eqs. (4,5) in the next section to build an estimation algorithm to assess bubble size in bread dough.

3. Materials and methods

3.1. Sample preparation and experimental procedure

Bread dough samples were obtained by mixing 2000 g of wheat flour (Type 55, Moulins Soufflet Pantin), 1140 g of water, 40 g of salt, 20 g of improver and 100 g of yeast (optional) in a Moretti Forni Grain Spiry 8 dough mixer for 17 min at 100 rotations per minute. The advantages of using non-yeasted dough were to provide a stable object with regard to the acquisition time, with possible comparison of structure with yeasted dough at the initial time of proving. A fraction of gas (mainly air) is incorporated at the mixing stage and porosity at the end of mixing was estimated at 10 ± 2% depending on the mixer used for a given recipe [32], with a mean gas bubble size of approximately 0.05 mm to 0.3 mm [22].

Dough temperature and water content were checked for the evaluation of the reproducibility between batches as both are known to affect the relaxation signal of dough [29, 30]. The temperature was 24.5 ± 0.5°C, and water content was 45 ± 3 g of water per 100 g of dough. Cylindrical flasks (Ø = 50 mm, 70 mm height) were filled with 50 g of yeasted dough or 100 g of non-yeasted dough. A lid was placed over the flask to limit dehydration during measurement. Flasks were then placed in a tunnel within the magnet, equipped with thermal regulation set at 24.5°C. Internal tunnel temperature was monitored with thermocouples. MRI acquisitions were begun at approximately t= 7 min, t=0 referring to the end of mixing.

Cylindrical flasks were also filled with $MnCl_2$ solution, the concentration (1287.2 µM) being adjusted to obtain a T_2 value close to that of bread dough, i.e. $T_2 = 20$ ms. SE images of the phantom were used to normalize dough MR images to correct for inherent magnet and coil spatial inhomogeneities.

3.2. MRI device and parameters

A 0.2 T electromagnet scanner in open configuration (Magnetom Open, Siemens, Erlangen, Germany) equipped with a head coil was used to image the bread dough. Double GE sequences (TE_1 = 4 ms, TE_2 = 12 ms) were performed to assess signal loss and $T_2\chi$ during dough proving. SE sequences (TE = 8 ms) were used to obtain local porosity. For all sequences, slice thickness (*ST*), bandwidth (*BW*), field of view (*FOV*), matrix size (*N*), number of accumulations (*Acc*) and repetition time (*TR*) were set as follows: *ST* = 5 mm, *BW* = 279 Hz/pixel, *FOV* = 128 x 128 mm^2, *N* = 128x128, *Acc* = 4, *TR* = 300 ms. Each sequence lasted 2 min 33 s, and GE and SE sequences were alternated.

3.3. Porosity map

Assuming an initial uniform porosity at a reference time, the porosity of a voxel (i, j) can be estimated from its gray level during proving in SE imaging [18]:

$$\varepsilon(i,j) = 1 - (1 - \varepsilon_{init}).\frac{SE(i,j)}{MGL_{init}} \quad (6)$$

with ε_{init} the initial overall porosity (ε_{init} = *10%)* at t_{init} = 9.5 min, i.e. the time to obtain the first SE image, MGL_{init} the corresponding mean gray level computed on a reference ROI, and *SE(i,j)* the gray level in the SE image at the location (i,j). We verified that the mean value computed in the porosity map was concordant with the overall porosity computed from the total dough volume measurement.

3.4. $T_2\chi$ map

With $GE_1(i,j)$ and $GE_2(i,j)$ as the GE images at TE_1 and TE_2, the $T_2\chi$ map can be defined as follows:

$$T_{2\chi}(i,j) = \frac{(TE_2 - TE_1)}{\ln(\frac{GE_1(i,j)}{GE_2(i,j)})} \quad (7)$$

In fact, the exponential signal decay constant was estimated from two points only. Prior simulations showed that $TE_1 = 4\ ms$ and $TE_2 = 12\ ms$ were suitable for a 0.2 T magnetic field.

3.5. Bubble size estimation algorithm

The algorithm principle was to combine $T_2\chi$ and porosity maps to estimate local bubble radii. Indeed, from Eq. (4) we can extract bubble radii (r) and compute the map of radii *r(i,j)* according to Eq. (8):

$$r(i,j) = r_{break}(i,j) - \frac{1}{\lambda(i,j)}.\ln\left(\frac{K(i,j)}{T_{2\chi}(i,j) - T_{2\chi_{init}}(i,j)} - 1\right) \quad (8)$$

r_{break}, K, λ and $T_2\chi_{init}$ were determined for each pixel from the porosity map using Eq. (5).

$T_2\chi$ was simulated from a set of several bubbles, i.e. signal loss was characterized in the center of the image to take into account the influence of the neighboring bubbles. This local approach based on several voxels should result in a coherent estimation algorithm, and therefore *r(i,j)* was not directly computed pixel-by-pixel but through a 3x3 averaging mask. This allowed replacement of the pixel value by a local average around the pixel of interest. Indeed, the non-linear property of the logarithm function made the subsequent use of an averaging on the map of radii impossible. Prior to computation of Eq. (8), we therefore applied the mask on r_{break}, K, λ, $T_2\chi$ and $T_2\chi_{init}$ maps.

4. Results

4.1. Non- yeasted dough

The porosity map of the non-yeasted dough was computed according to Eq. (6) and is represented in Fig. 4. The largest bubbles were easily detectable and the rest of the dough was quite uniform and dense. Mean porosity on a large reference ROI was found to be 12.6%. The corresponding mean value in the $T_2\chi$ map computed on the same ROI was 12.9 ms. Compared

284 with simulation results ($T_2\chi$ = 13 ms and ε = 12.5 % in Fig. 2.a), these two values were in
285 good agreement. The T_2 value of bread dough used for simulation and the general hypothesis
286 of regularly spaced bubbles were justified to reach a good order of magnitude. The bubble
287 size estimation algorithm was then applied to obtain the map of radii depicted in Fig. 5. The
288 large bubbles were even more clearly revealed due to increased contrast compared to the
289 neighboring environment. Fig.5 also demonstrates localized regions of smaller bubbles which
290 were hardly visible in the porosity map (Fig. 4). The map of radii depicted different regions
291 corresponding to different bubble sizes. Smaller bubbles can be seen surrounded by larger
292 bubbles, themselves surrounded by larger bubbles and so on. This radius evolution was
293 spatially reproduced on the dough area, leading to different visible networks. The histogram
294 representing the number of pixels according to their estimated radii extracted from the
295 reference ROI is presented in Fig. 6. A Gaussian probability density function was found to fit
296 well the experimental distribution of bubble size, as shown in Fig. 6 (σ = 0.062, μ = 0.37, R^2 =
297 0.991 with TableCurve2D® software, Jandel Scientific, version 5). The mean value computed
298 in the reference ROI of the *r(i,j)* map was r = 0.38 pix_{ima}. As detailed in the discussion
299 section, estimated radius values were subjected to certain limits inherent to the method and
300 values were not systematically significant. However, they can provide relative information
301 about spatial differences (for a given protocol) and between different protocols of dough
302 production.

303 *4.2. Dough during proving*

304 As in the previous experiment with the non-yeasted dough, *r(i,j)* was then computed for
305 dough during proving. The three first maps at t_1 = 7 min, t_2 = 12.5 min and t_3 = 18 min after
306 completing mixing are represented in Fig. 7 on the same scale as Fig. 5. Histograms were
307 computed at t_1, t_2 and t_3, taking the same reference ROI occupying almost all the dough at t_1
308 (Fig. 8). As in the non-yeasted dough, distributions were Gaussian and shifted to the higher

radius during proving, consistent with the growth of bubbles under desolubilization/vaporization of CO_2, ethanol and water vapor. The average radius estimated from the algorithm as a function of the proving time is also presented in Fig. 9. Bubble size distribution was slightly shifted compared to non-yeasted dough, which may be attributed to the start of fermentation between the end of mixing and the first MRI acquisition (see Materials and Methods section). At t_2, modification in the dough structure was clearly observed (Fig. 7.b). Groups of bubbles were growing and were identifiable from t_1 to t_3 and also for longer proving times. The overall networks, i.e. virtual limits between regions of the same radius, seemed to be almost unchanged in the horizontal direction during proving while bubbles underwent overall growth. From Fig. 7 and a complete set of maps of radii, dough evolution seemed to be related to the starting structure of the dough. Image processing methods on maps of radii would be useful for tracking purposes.

5. Discussion

In this section, we first discuss the simulation of $T_2\chi$ and the behavior of the signal. We then explain the limitations of the method. Finally, results on non-yeasted dough and dough during proving will be analyzed in the light of this previous discussion.

5.1. Simulated evolution of $T_2\chi$

Simulation results concerning $T_2\chi$ as a function of bubble radius (Fig. 2) were original and to our knowledge have never been reported in the literature. Several studies have been undertaken to study NMR signal dephasing due to the presence of mesoscopic field inhomogeneities in the static dephasing regime [25, 26]. The relaxation constant was thus found to be independent of cylinder or bubble radii. From the free induction decay due to randomly distributed spherical particles, Yablonskiy [33] derived an expression for the relaxation rate $R_2^{\#}$ defined in section 2.1:

$$R_2^{\#} = \frac{4\pi}{9\sqrt{3}} \varepsilon.\gamma.\Delta_\chi.B_0 \quad (9)$$

Eq. (9) explains $T_2\chi$ shortening with increasing porosity (Fig. 3.a) or main magnetic field (Fig. 2.b), and the values are compatible with our present study. Indeed, if ε = 12.6%, Eq. (9) resulted in $T_2^* = 1 / (R_2 + R_2^{\#})$ = 12.2 ms and $T_2\chi$ = 13 ms in our simulation.

We demonstrated three levels for $T_2\chi$ observation. First, the plateau in Fig. 2.a indicated that, for a given porosity (or density), $T_2\chi$ values are independent of bubble radii. This confirmed all the results encountered in mesoscopic scale studies. We showed that $T_2\chi$ was dependent on radius in a certain range (macroscopic scale) and thus constitutes a sensitive indicator of the medium alveolar structure. The second plateau occurred for large bubbles compared to voxel size. $T_2\chi$ was higher for larger bubbles because the signal from an air voxel could not decrease with *TE* due to the almost total absence of signal. In fact, heterogeneity was high in the ROI corresponding to the second plateau with complete air voxels, whereas for the first plateau each voxel contained small air bubbles. There were therefore more susceptibility interfaces for small bubbles, thus explaining the lower $T_2\chi$ values. At a constant radius, an increase in porosity means a reduction in the center to center distance (*ccd*) and thus intravoxel dephasing is greater, as described in [27] and in Eq. (1), explaining the decrease of $T_2\chi$ with porosity.

Simulations at 1.5 T (Fig. 2.b) showed the potential of this method since there was a greater difference between $T_2\chi_{init}$ values for low porosities and an augmentation of the *K* factor. By using Eq. (8) to reveal bubbles, the estimated radius dynamic is thus enlarged and the algorithm would be more stable. Furthermore, a major gain in signal at high field would make better resolution possible. This is valuable for the study of the very small bubbles present in non-yeasted dough. Indeed, Bellido et al. reported a mean value of 100 μm in wheat flour dough [16].

5.2. *Limitations of the method*

Fig 2.a illustrates some drawbacks of the method. $T_2\chi$ is the same for small radii constituting the first plateau. Bubbles within this range cannot be discriminated. Fortunately, the process of dough proving with the growth of bubbles and the increase in local porosity was suited to this sensitive domain. Due to the shape of the $T_2\chi$ curve (Fig. 2.a), computation of *r(i,j)* according to Eq. (8) worked well in the dynamic area between the two plateaux.

Although bread dough structure is highly heterogeneous (gaseous phase and dough films included), the model was quite accurate in terms of signal loss. A more accurate virtual description of the object will undoubtedly make possible the calculation of values of greater accuracy. In fact, the expansion of bubbles rapidly becomes heterogeneous and anisotropic (non-spherical and distorted bubbles) due to mechanisms of coalescence [23]. However, using the estimation algorithm, it is possible to distinguish between bubbles according to their radius. At this point, *r(i,j)* values have to be considered as variables related to length rather than a physical variable. Babin et al. [22] found dough structures were heterogeneous and dependent on the recipe, with bubble radii in the range 0.05-0.3 mm at the very beginning of dough proving. Maps of the radii in the present study were thus thought to be overestimated.

5.3. *Non-yeasted dough and dough during proving*

There is a real value in combining SE and GE sequences to assess local porosity and signal loss and thus deduce bubble radii. A porosity map (Fig. 4) provides important information (density is a criterion used by bakers to distinguish between bread recipes or to evaluate defects originating from the flour or the different stages in bread making) but a map of radii (Fig. 5) supplements the scientific understanding of evolution of the dough structure, from small to large bubbles. Additionally, the field of view available with MRI offers the possibility of assessing macroscopic heterogeneities (scale of a few millimeters to centimeters) in samples of realistic size comparable with industrial practices. Several image

processing techniques based on this map could be developed to classify or segment bubbles. The histogram presented in Fig. 6 shows a Gaussian distribution of bubbles. Bellido et al. [16] used microcomputed tomography on dough and found a log-normal distribution. These first results were encouraging for the study of non-yeasted bread dough.

Bikard et al. [23] analyzed the foaming phase during proving using 3D simulation. They characterized the influence of parameters such as dough viscosity, kinetics or initial number of bubbles on the evolution of average bubble radius over time. Fig. 9 obtained from maps of radii at different times of proving is in good agreement with their results while looking at curve shapes. From a quantitative point of view, it was hard to compare as values were highly dependent on the above parameters that we could not quantify in our experiments.

Using digital image analysis, Rouille et al. [34] showed that reduction in the number of small bubbles (Ø < 1 mm) was proportionally balanced by an increase in the number of larger bubbles (1 mm < Ø < 2 mm) during proving. This is also obvious from Figs. 7-8.

Image analysis-based methods [17, 20] showed limitations due to small sample size (magnetic resonance microscopy) and long imaging times. Even for small pixel size (115 µm), resolution is not sufficient to detect small bubbles at the beginning of the proving time [34]. Susceptibility-based methods are able to reveal information at a lower scale due to the expansion of field inhomogeneities and associated signal loss.

6. Conclusion

Because they arise from object-dependent field inhomogeneities, magnetic susceptibility effects can be a source of quantitative data to characterize alveolar products such as bread dough. While classic image analysis techniques are limited by image or temporal resolution, this new method combines local porosity, local signal loss and simulation predictions to assess bubble radii which can be smaller or the same order of magnitude than the voxel. However, fully quantitative accuracy of the method would suppose comparisons between

different techniques or the use of a test object with known geometry and susceptibility. Moreover, further simulation studies with more realistic object geometries to mimic bread dough would make possible more quantitative results. Growth and distribution of bubbles were observed during proving. Maps of radii gave information about dough structure and evolution. The principle of the estimation algorithm was shown at 0.2 T and simulations predicted greater distinction between bubble sizes at 1.5 T, especially for low porosities which are also encountered at key stages in breadmaking.

Acknowledgments

The authors would like to thank D. Le Ray for dough preparations and the Regional Council of Brittany for financial support.

References

[1] Ludeke KM, Roschmann P and Tischler R. Susceptibility artefacts in NMR imaging. Magn Reson Imaging 1985;3:329-343.

[2] Bakker CJG, Bhagwandien R, Moerland MA and Ramos LMP. Simulation of susceptibility artifacts in 2D and 3D Fourier transform spin-echo and gradient-echo magnetic resonance imaging. Magn Reson Imaging 1994;12:767-774.

[3] Fernandez-Seara MA and Wehrli FW. Postprocessing technique to correct for background gradients in image-based R2* measurements. Magn Reson Med 2000;44:358-366.

[4] Ogawa S, Menon RS, Tank DW, Kim SG, Merkle H, Ellermann JM and Ugurbil K. Functional brain mapping by blood oxygenation level-dependent contrast magnetic resonance imaging. A comparison of signal characteristics with a biophysical model. Biophys J 1993;64:803-812.

[5] Haacke EM, Xu YB, Cheng YCN and Reichenbach JR. Susceptibility weighted imaging (SWI). Magn Reson Med 2004;52:612-618.

[6] Sehgal V, Delproposto Z, Haacke EM, Xu Y, Neelavalli J, Haddar D, Tong KA, Wycliffe N, Kido DK and Reichenbach JR. Clinical applications of neuroimaging with susceptibility-weighted imaging. J Magn Reson Imaging 2005;22:439-450.

[7] Cunningham CH, Arai T, Yang PC, McConnell MV, Pauly JM and Conolly SM. Positive contrast magnetic resonance imaging of cells labeled with magnetic nanoparticles. Magn Reson Med 2005;53:999-1005.

[8] Bos C, Delmas Y, Desmouliere A, Solanilla A, Hauger O, Grosset C, Dubus I, Ivanovic Z, Rosenbaum J, Charbord P and others. In vivo MR imaging of intravascularly injected magnetically labeled mesenchymal stem cells in rat kidney and liver. Radiology 2004;233:781-789.

[9] Ittrich H, Lange C, Togel F, Zander AR, Dahnke H, Westenfelder C, Adam G and Nolte-Ernsting C. In vivo magnetic resonance imaging of iron oxide-labeled, arterially-injected mesenchymal stem cells in kidneys of rats with acute ischemic kidney injury: Detection and monitoring at 3T. J Magn Reson Imaging 2007;25:1179-1191.

[10] Mowat P, Franconi F, Chapon C, Lemaire L, Dorat J, Hindre F, Benoit JP, Richomme P and Le Jeune JJ. Evaluating SPIO-labelled cell MR efficiency by three-dimensional quantitative T-2* MRI. NMR Biomed 2007;20:21-27.

[11] Beuf O, Briguet A, Lissac M and Davis R. Magnetic resonance imaging for the determination of magnetic susceptibility of materials. Journal of magnetic resonance. Series B 1996;112:111-118.

[12] Peeters JM, van Faassen EEH and Bakker CJG. Magnetic resonance imaging of microstructure transition in stainless steel. Magn Reson Imaging 2006;24:663-672.

[13] Robson P and Hall L. Identifying particles in industrial systems using MRI susceptibility artefacts. AIChE Journal 2005;51:1633-1640.

[14] Wong KK, Huang I, Kim YR, Tang H, Yang ES, Kwong KK and Wu EX. In vivo study of microbubbles as an MR susceptibility contrast agent. Magn Reson Med 2004;52:445-452.

[15] Niranjan K. An Introduction to Bubble Mechanics in Foods. In: Campbell GM, Webb C, Pandiella SS, Niranjan K, editors. Bubbles in Food. St Paul: Eagan Press, 1999. p. 3-9.

[16] Bellido GG, Scanlon MG, Page JH and Hallgrimsson B. The bubble size distribution in wheat flour dough. Food Res Int 2006;39:1058-1066.

[17] Bonny J-M, Rouille J, Della Valle G, Devaux M-F, Douliez J-P and Renou J-P. Dynamic magnetic resonance microscopy of flour dough fermentation. Magn Reson Imaging 2004;22:395-401.

[18] Grenier A, Lucas T, Collewet G and Le Bail A. Assessment by MRI of local porosity in dough during proving. Theoretical considerations and experimental validation using a spin-echo sequence. Magn Reson Imaging 2003;21:1071-1086.
[19] Ishida N, Takano H, Naito S, Isobe S, Uemura K, Haishi T, Kosse K, Koizumi M and Kano H. Architecture of baked breads depicted by a magnetic resonance imaging. Magn Reson Imaging 2001;19:867-874.
[20] van Duynhoven JPM, van Kempen GMP, van Sluis R, Rieger B, Weegels P, van Vliet LJ and Nicolay K. Quantitative assessment of gas cell development during the proofing of dough by magnetic resonance imaging and image analysis. Cereal Chem 2003;80:390-395.
[21] Wagner MJ, Loubat M, Sommier A, Le Ray D, Collewet G, Broyart B, Quintard H, Davenel A, Trystram G and Lucas T. MRI study of bread baking: Experimental device and MRI signal analysis. International Journal of Food Science and Technology 2008;43:1129-1139.
[22] Babin P, Della Valle G, Chiron H, Cloetens P, Hoszowska J, Pernot P, Re?guerre AL, Salvo L and Dendievel R. Fast X-ray tomography analysis of bubble growth and foam setting during breadmaking. Journal of Cereal Science 2006;43:393-397.
[23] Bikard J, Coupez T, Della Valle G and Vergnes B. Simulation of bread making process using a direct 3D numerical method at microscale: Analysis of foaming phase during proofing. J Food Eng 2008;85:259-267.
[24] Babin P, Della Valle G, Dendievel R, Lourdin D and Salvo L. X-ray tomography study of the cellular structure of extruded starches and its relations with expansion phenomenon and foam mechanical properties. Carbohydrate Polymers 2007;68:329-340.
[25] Yung K-T. Empirical models of transverse relaxation for spherical magnetic perturbers. Magn Reson Imaging 2003;21:451-463.
[26] Sukstanskii AL and Yablonskiy DA. Theory of FID NMR signal dephasing induced by mesoscopic magnetic field inhomogeneities in biological systems. J Magn Reson 2001;151:107-117.
[27] De Guio F, Benoit-Cattin H and Davenel A. Signal decay due to susceptibility-induced intravoxel dephasing on multiple air-filled cylinders: MRI simulations and experiments. Magn Reson Mater Phy 2008;21:In press.
[28] Benoit-Cattin H, Collewet G, Belaroussi B, Saint-Jalmes H and Odet C. The SIMRI project: a versatile and interactive MRI simulator. J Magn Reson 2005;173:97-115.
[29] Ruan RR, Wang XA, Chen PL, Fulcher RG, Pesheck P and Chakrabarti S. Study of water in dough using nuclear magnetic resonance. Cereal Chem 1999;76:231-235.
[30] Grenier A, Lucas T, Davenel A, Cambert M, Le Bail A and Mariette F. Assessment of NMR relaxation times and ice fraction in frozen dough. J Agr Food Chem 2008:submitted.
[31] Lodi A, Abduljalil AM and Vodovotz Y. Characterization of water distribution in bread during storage using magnetic resonance imaging. Magn Reson Imaging 2007;25:1449-1458.
[32] Cauvain SP, Whitworth MB and Alava JM. The Evolution of Bubble Structure in Bread Doughs and Its Effect on Bread Structure. In: Campbell GM, Webb C, Pandiella SS, Niranjan K, editors. Bubbles in Food. St Paul: Eagan Press, 1999. p. 85-88.
[33] Yablonskiy DA. Quantitation of intrinsic magnetic susceptibility-related effects in a tissue matrix. Phantom study. Magn Reson Med 1998;39:417-428.
[34] Rouillé J, Della Valle G, Devaux MF, Bonny J-M and Renou JP. Effect of flour minor components on bubble growth in bread dough during proofing assessed by magnetic resonance imaging. J Agr Food Chem 2005;53:3986-3994.

Figure legends

Figure 1: Overview of simulation framework. Field inhomogeneities map was dependent on object parameters (r, ccd, $\Delta\chi$, Nb) and was an input of MRI simulator SIMRI. $T_2\chi$ was determined for each object from ROI in GE simulated images at different TE from 4 to 12 ms.

Figure 2: $T_2\chi$ value as a function of bubble radii at different porosities with sigmoid fitting curves. **a)** At B_0 = 0.2 T. **b)** At B_0 = 1.5 T. Three stages were identified: an initial plateau where $T_2\chi$ was only dependent on porosity (density), a rapid increase in $T_2\chi$ value and a second plateau corresponding to high air proportion in voxels.

Figure 3: **a)** K and $T_2\chi_{init}$ as functions of porosity. **b)** r_{break} and λ as functions of porosity. Second order polynomial relationship with porosity was found for each simulation parameter.

Figure 4: Porosity map of non-yeasted bread dough. Large bubbles can be distinguished as high-value pixels. The squared reference ROI is represented.

Figure 5: Map of estimated radii of bubbles in non-yeasted bread dough. Contrast enhancement between the different regions of bubble sizes highlighting dough structure with small bubbles surrounded by larger bubbles, etc.

Figure 6: Histogram with Gaussian distribution (σ = 0.062, μ = 0.37, R^2 = 0.991) of the non-yeasted dough computed on the reference ROI with a 0.02 pix_{ima} interval.

Figure 7: Map of estimated radii of bubbles in bread dough during proving. **a)** At t = 7 min **b)** At t = 12.5 min **c)** At t = 18 min showing distribution and growth of bubbles.

Figure 8: Histograms extracted from maps of radii showing distribution of bubble sizes at three proving times.

Figure 9: Average estimated radius as a function of proving time.

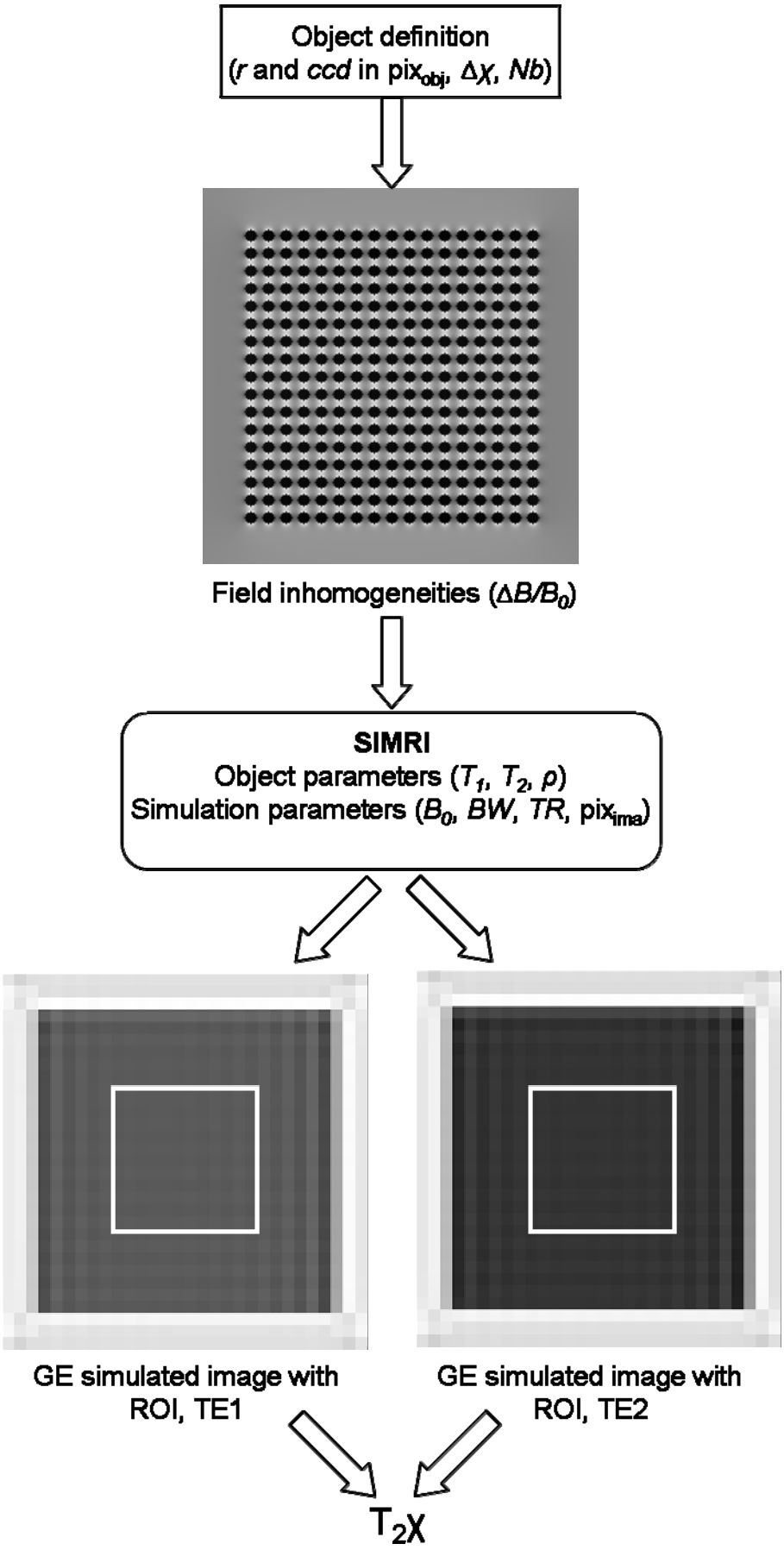
Object definition
(r and ccd in pix_obj, Δχ, Nb)
Field inhomogeneities (ΔB/B_0)
SIMRI
Object parameters (T_1, T_2, ρ)
Simulation parameters (B_0, BW, TR, pix_ima)
GE simulated image with ROI, TE1
GE simulated image with ROI, TE2
T_2χ

533

534 Fig.1

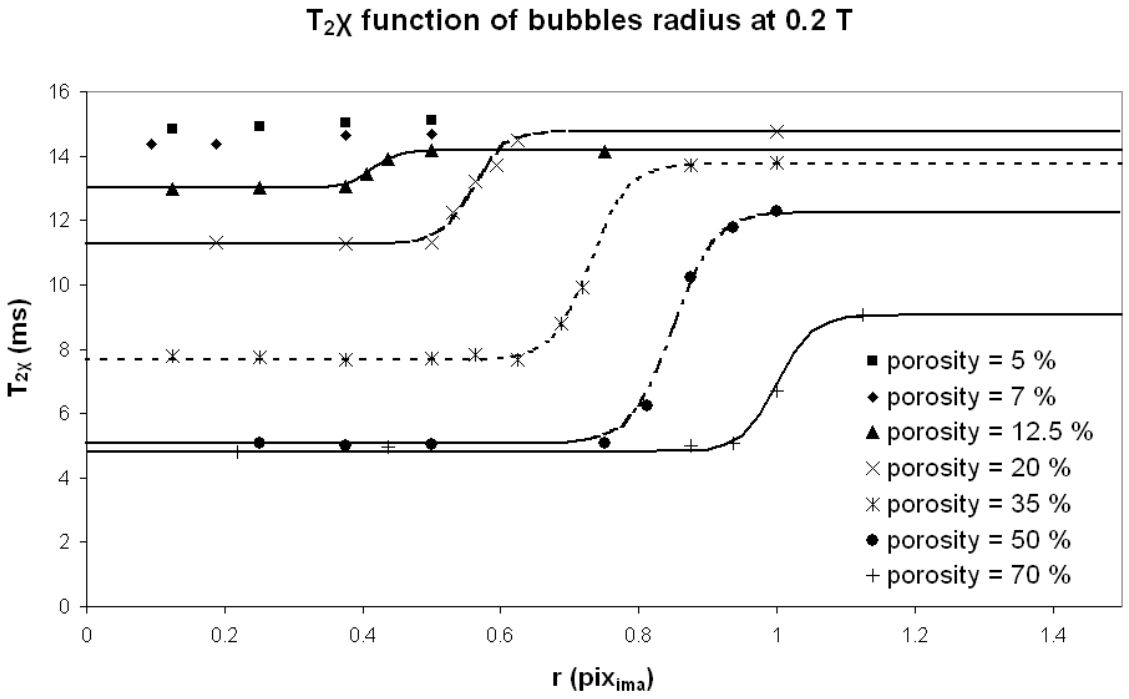

535

536 Fig2a

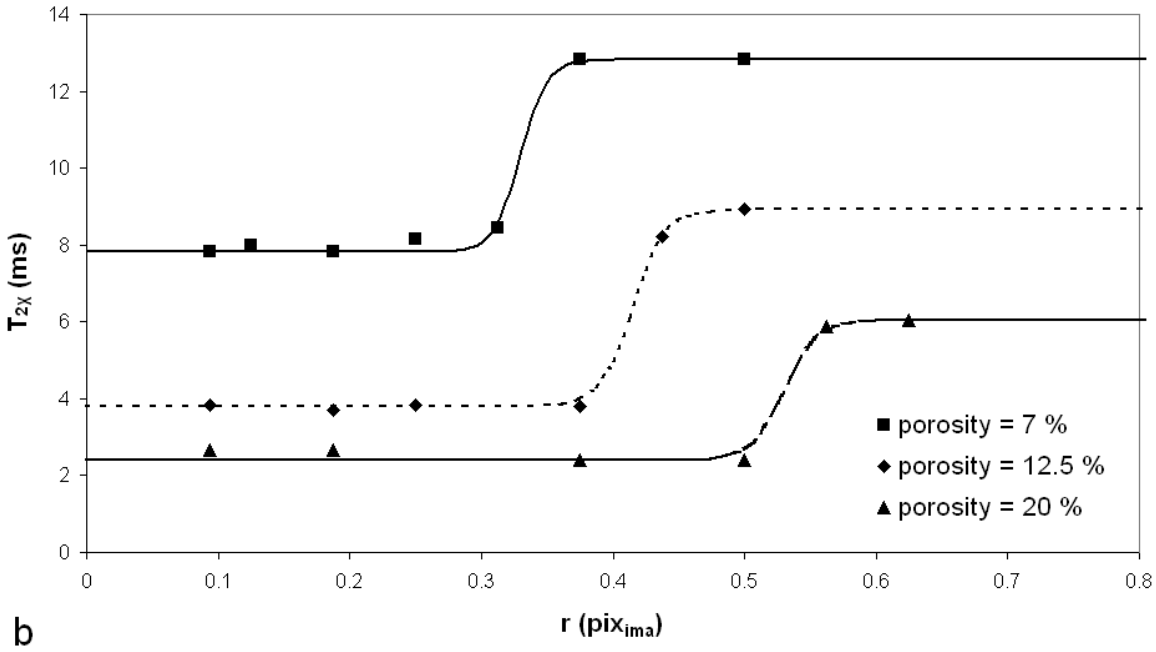

b

537

538 Fig.2b

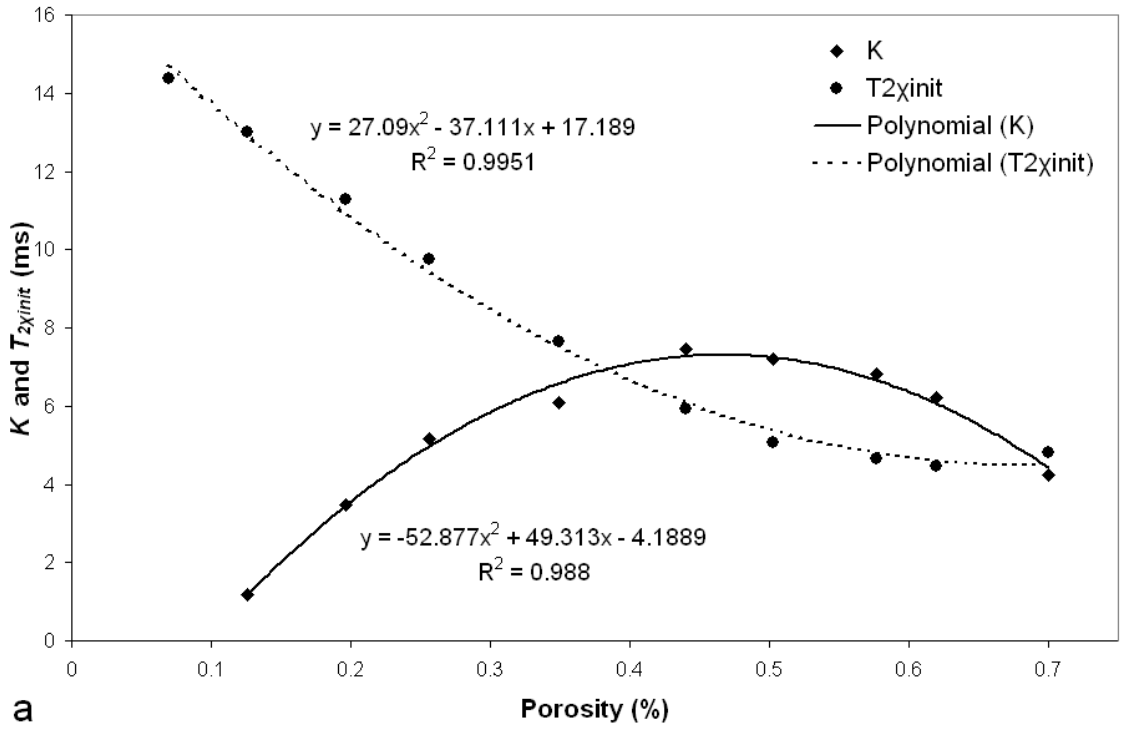

539

540 Fig.3a

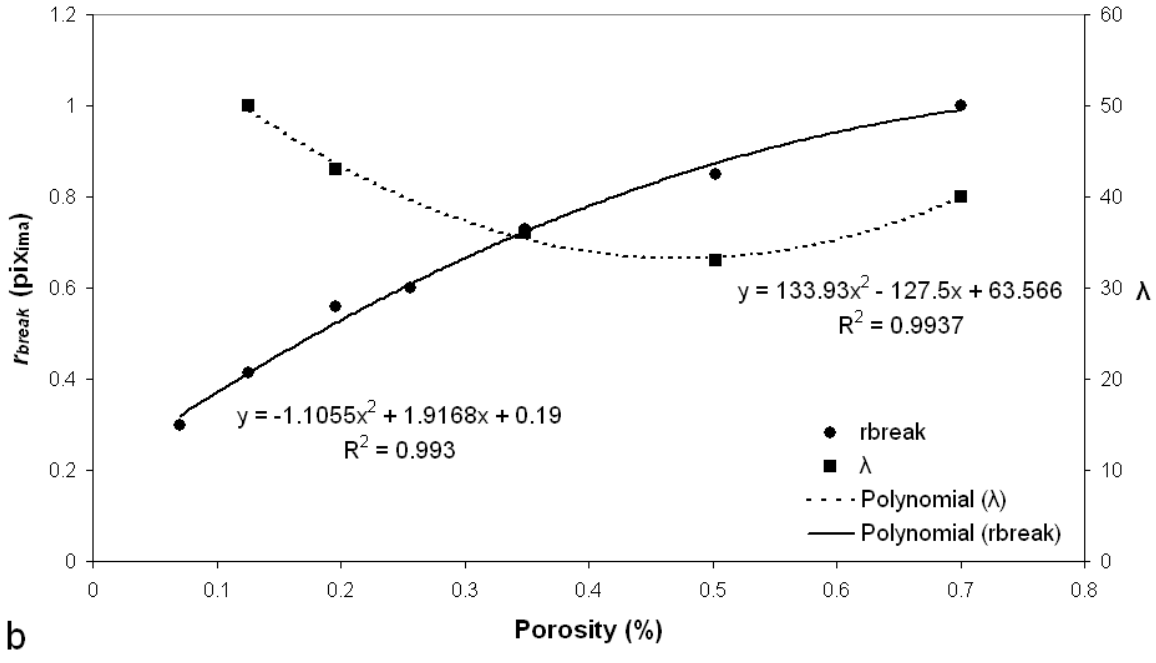

541

542 Fig.3b

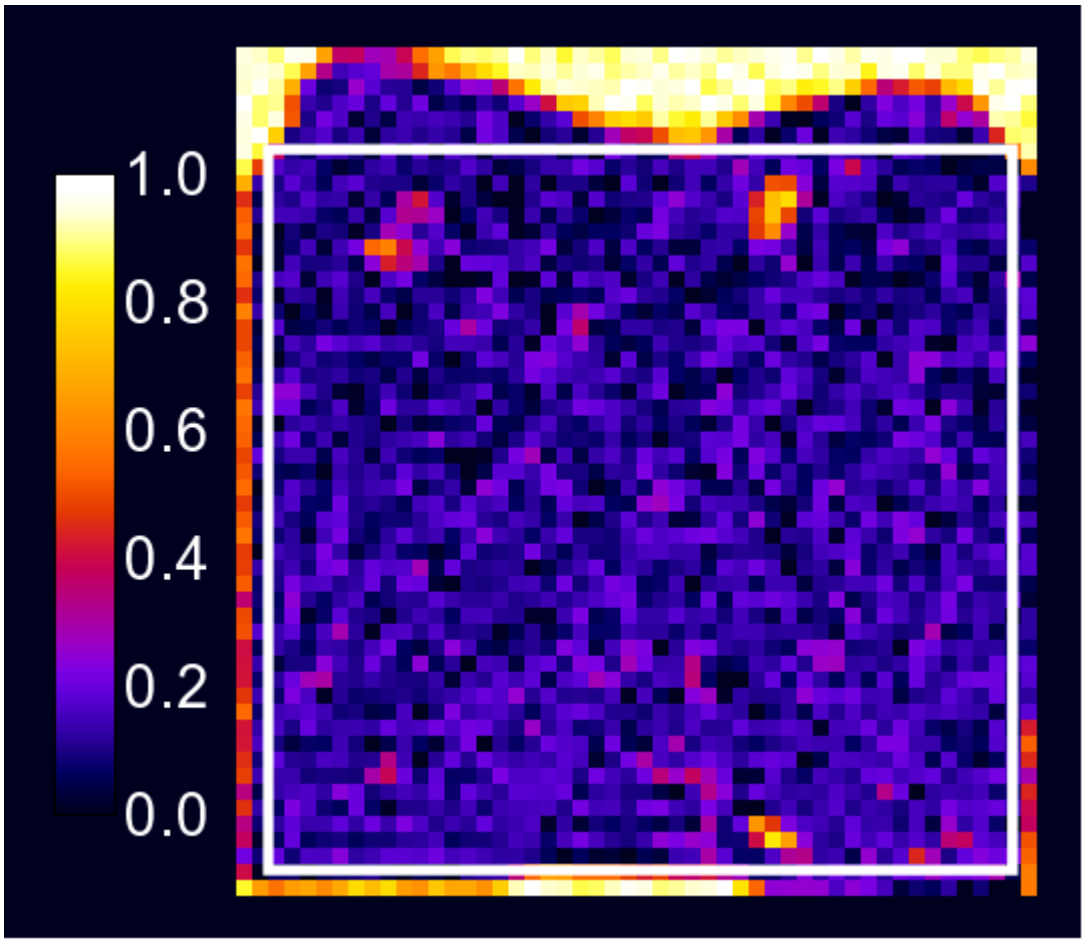

543

544 Fig.4

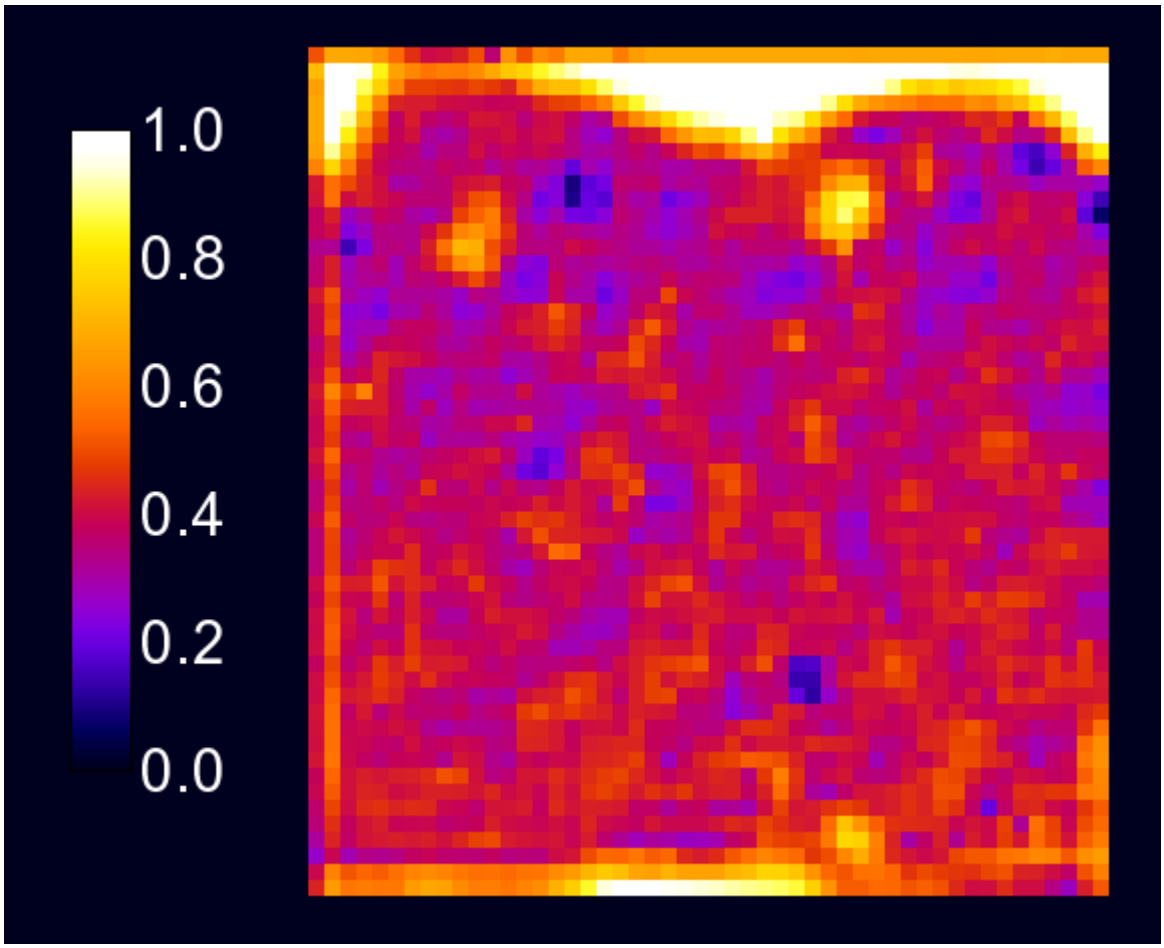

Fig.5

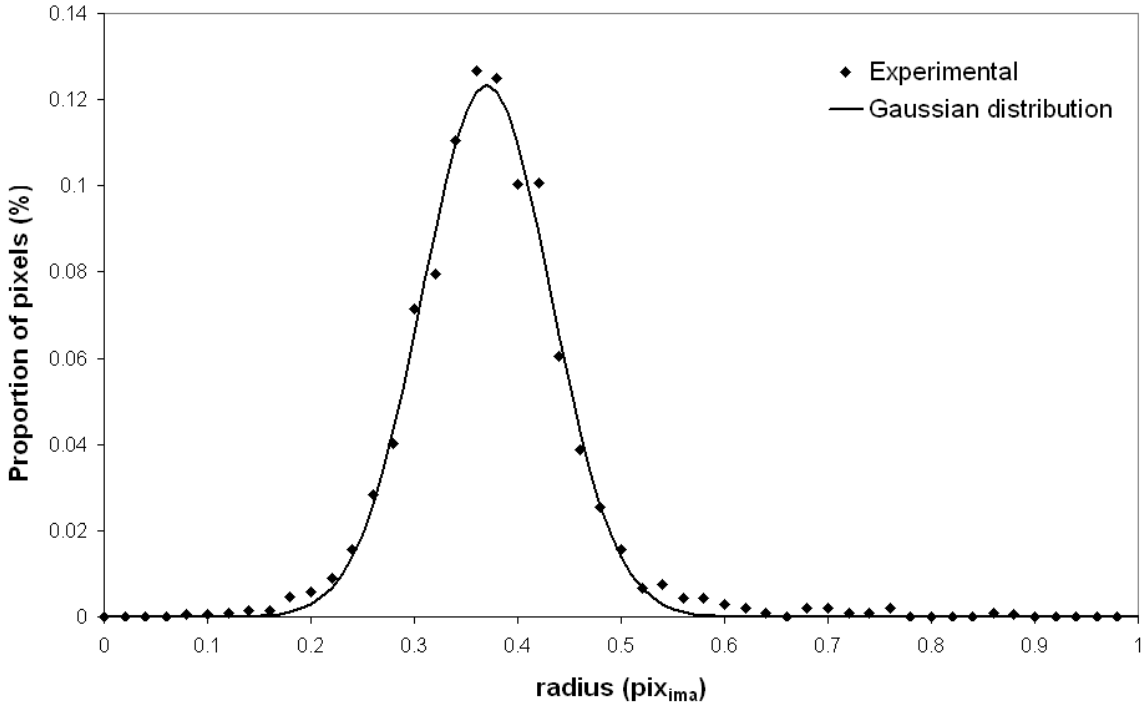
Experimental
Gaussian distribution
Proportion of pixels (%)
radius (pix$_{ima}$)
0.14
0.12
0.1
0.08
0.06
0.04
0.02
0
0
0.1
0.2
0.3
0.4
0.5
0.6
0.7
0.8
0.9
1

547

548 Fig.6

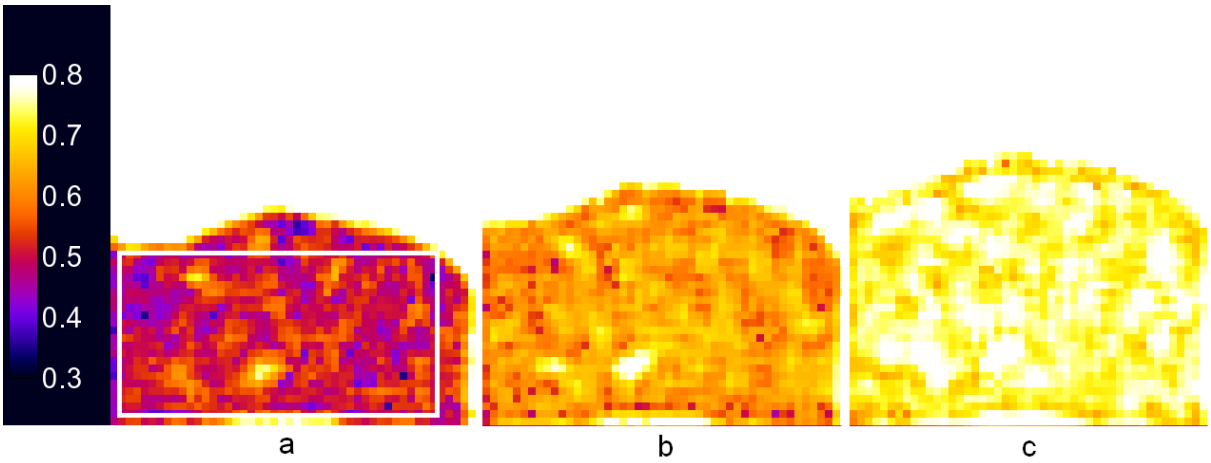

549

550 Fig7

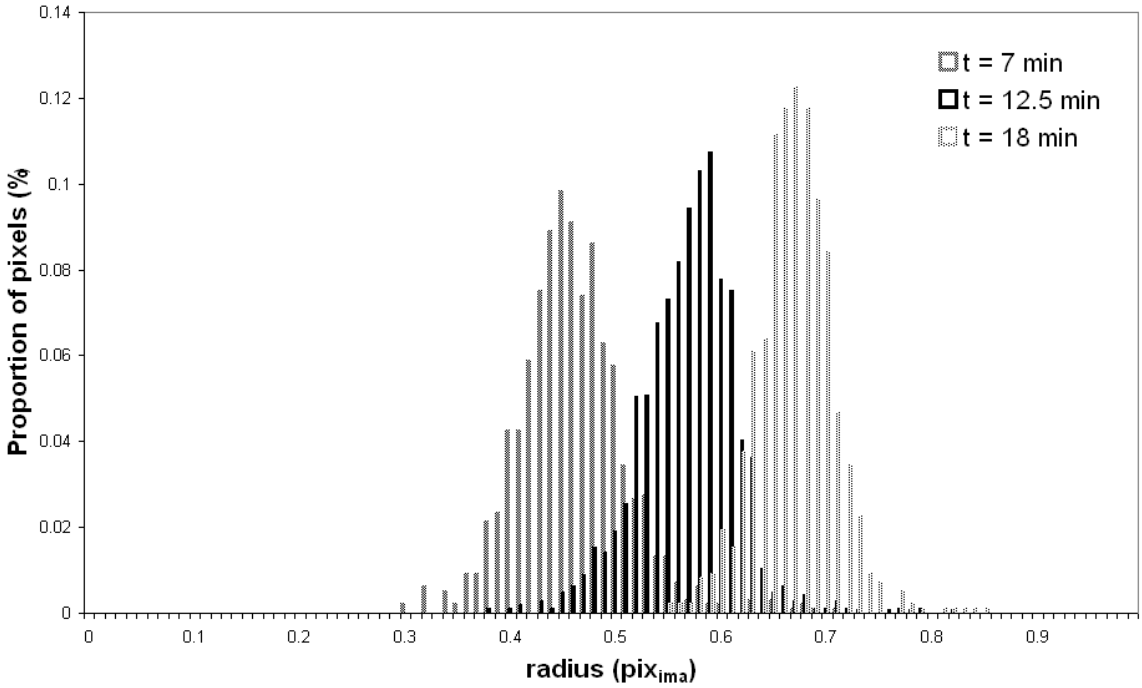
0.14
0.12
0.1
0.08
0.06
0.04
0.02
0
Proportion of pixels (%
0
0.1
0.2
0.3
0.4
0.5
0.6
0.7
0.8
0.9
radius (pix$_{ima}$)
t = 7 min
t = 12.5 min
t = 18 min

551

552 Fig.8

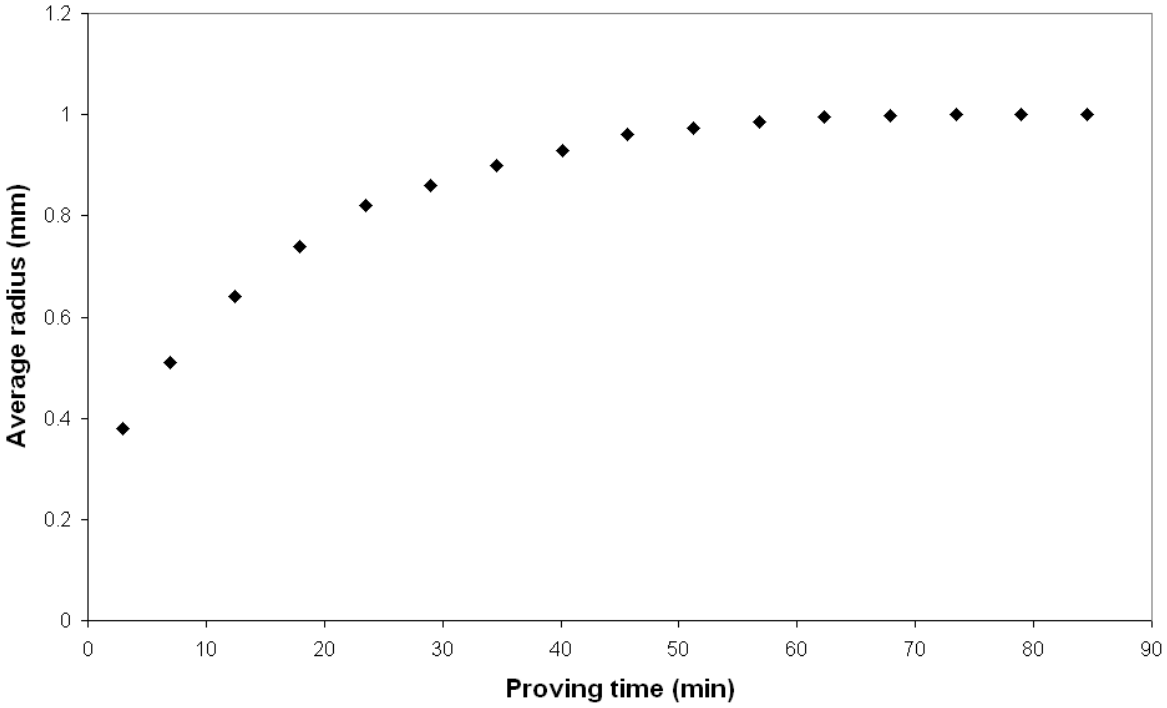

553

554 Fig.9

555